Qualification of Image-Based Measurement Systems for Characterization of Sprays

Jonas Schulz[1], Christoph Schunk[2], Eckhard Schleicher[2], and Hans-Jörg Bart[1,*]

DOI: 10.1002/cite.202000104

Image-based measurement techniques become increasingly popular and expedite digitalization in chemical engineering. This article demonstrates their potential by testing two inline probes, namely modified optical multimode online probe (OMOP) and process microscope. Validations are performed with static monodisperse standards (9.2 µm to 406 µm) and fast-moving droplets (68.6 µm to 860.7 µm; 24.5 m s^{-1} to 11 m s^{-1}). Screening of a lithography attests both probes great distortion-free image quality. A 1951 USAF chart attests a low optical resolution of 8 µm or 7 µm with respect to the OMOP or process microscope, respectively. The modified OMOP and process microscope reaches accuracies of 7.6 % or 5.9 % for particles and 8.2 % or 6.8 % for droplets.

Keywords: Droplet detection, Image analysis, Optical measurement, Particle analysis, Spray analysis

Received: May 12, 2020; *revised:* October 19, 2020; *accepted:* November 10, 2020

1 Introduction

Optical measurement methods for spray and droplet swarm analysis are rare and not widespread applied in industry but often found in research and development. Nevertheless, the availability of cheaper sensors and the start of digitalization in chemical engineering has the potential to use the large amount of data generated by optical measurement systems to advance process control significantly by enhanced data analysis and improved communication between single devices [1]. Ongoing research projects *(wanted-technologies.de),* as for example ERICAA (BMWi; FKZ 03ET1391F) and TERESA (BMWi; FKZ 03ET1395H) apply image-based measurement techniques to deepen the understanding of hydrodynamics in separation plants and thus release new impulses for apparatus control and design. While research shows first success in application of image-based measurement techniques in liquid-liquid systems [2, 3], the analysis of sprays has a favorable start [4, 5]. Besides development and application of an image-based measurement technique for spray analysis [6] potential users are also interested in the reliability and validity of the respective instrument. Hence, this article covers the performance of image-based measurement systems for spray detection in terms of optical resolution margins, accuracy, and velocity. Detection and analysis of monodisperse glass particles and water droplets allow a reasonable estimation of the qualification of latest imaging systems for a reliable spray analysis in pilot and industrial scale columns. For this purpose, two image-based measurement instruments, the process microscope from HZDR Innovation GmbH (HZDRI) and the modified optical multimode online probe (OMOP) developed by Technische Universität Kaiserslautern (TUK) are compared with each other. Direct comparisons based on experimental tests [3] remain rare and preceding articles rather focus on a qualitative evaluation of particle measurement methods [2, 7, 8]. With defined and constant test conditions, this article will emphasize the accuracy, performance and by that, the qualification of image-based measurement systems for the challenging spray analysis in industrial plants.

2 Image-Based Measurement Methods

Up to now, image-based measurement methods are rather applied in liquid-liquid [9, 10] and multiphase systems [11–13] together with bubble columns [14–16, 36]. Analysis of droplet dispersions in a surrounding gas phase remain scarce. An overview of available methods [4] reveals that only a few authors apply image-based measurement instruments for spray detection [17, 18]. Challenges, which impede a straightforward application, are at first an advanced design of the measurement probe and secondly the image analysis procedure. Published design concepts for these kind of image-based probes are young [5, 19], while

[1]Jonas Schulz, Prof. Dipl.-Ing. Dr. techn. Hans-Jörg Bart
bart@mv.uni-kl.de
Technische Universität Kaiserslautern, Chair of Separation Science and Technology, Gottlieb-Daimler-Straße 44, 67663 Kaiserslautern, Germany.
[2]Christoph Schunk, Eckhard Schleicher
HZDR Innovation GmbH, Bautzner Landstraße 400, 01328 Dresden, Germany.

particle image analysis represents a much discussed topic but rather with respect to bubbles [16, 20–22] and droplets [2, 23, 24] than sprays [4]. International standards for particle image analysis [25, 26] still focus on solid particles rather than sprays. In order to address this issue, this article delineates elements crucial for image analysis of liquid droplets in a continuous gas phase additionally to the aforementioned experimental comparison of both probes.

3 Material and Methods

3.1 Modified Optical Multimode Online Probe

The OMOP represents an image-based measurement probe, which combines transmitted light and telecentric optics in order to acquire images of droplets and bubbles rich in contrast with a high depth of field and an almost distance-independent object imaging [27]. The modified OMOP constitutes an advancement of the original instrument and enables the detection of sprays [28]. The original design of the OMOP comprises a cylindrical housing (D_{pr} = 38 mm; D_c = 150 mm) with an inspection window installed at the front of the probe [27]. The inspection window of the modified OMOP is hydrophobically coated and set back inside the cylindrical housing (D_{pr} = 35 mm; D_c = 450 mm) to prevent a coalescence with droplets of the spray. A pneumatic purging system enables cleansing of the inspection windows if required. Additional information regarding principle and construction are delineated in [4, 5]. The probe contains a Basler acA 1440-73gm area camera (1440×1080 pixels with 3.45 µm/pixel) and a telecentric lens from Edmund Optics (CompactTL™-series). The resulting field of view amounts to 4 mm×3.7 mm with an optical resolution of 8 µm. A high-power LED (Cree CXA series) enables an image acquisition at exposure times down to 1 µs. Latest probe design attaches the illumination to the camera unit by at the same time adjustable measurement volume and camera position. This endoscopic version of the shadowgraphic probe requires just one existing nozzle at the column shell as a measurement access [19].

3.2 Process Microscope

The process microscope of HZDR Innovation GmbH also works in trans-illumination mode and consists of two cylindrical units (D_{pr} = 20 mm). Both units access the test rig facing each other with a small gap of 6–10 mm using standard fittings like Swagelok®. The camera part applies a GigE-Vision camera system with a resolution of 656×492 pixels in grayscale with 8-bit color depth. The system reaches image acquisition rates up to 120 fps. Together with an achromatic lens pair from Edmund Optics (1:1,5, Effective Focal Length (EFL) 40/60 mm) the optical resolution is 6.6 µm. The focal plane of the probe is positioned 5 mm in front of the sapphire inspection window and spans a 3.5 mm×2.6 mm field of view with horizontal and vertical resolution of 5.3 µm/pixel. The illumination unit runs besides steady light also in double and alternating exposure, which enables velocity analysis of particles based on particle tracking beside the particle size measurement. The process microscope is controlled with a personal computer and a graphical control software, which allows image acquisition, adjustment of camera settings and the selection of several detection algorithms. In addition, the software possesses fundamental data analysis capabilities and supports plotting of particle size distributions. After analysis, the software provides plain text files (.csv), which can be easily processed using standard software like Excel® or Matlab®.

3.3 Experimental Setup and Examined Test Systems

In scope of this paper, an optical board (Thorlabs Inc.) and adjustment system (LT 80, OWIS GmbH) lay the foundation for the comparative measurements between both probes. The adjustment system enables an axially parallel alignment of camera and illumination unit to each other and a proper focusing of the examination object. Test systems for examination are a resolution test target (1951 USAF Test Target, Thorlabs Inc.), a lithographic pattern (TC-CB100, Technologie Manufaktur GmbH), monodisperse glass microspheres (Whitehouse Scientific Ltd.) and liquid monodisperse droplets ejected by a high precision droplet generator (FMP Technology GmbH). Fig. 1 depicts sample images of each test system for illustration.

The USAF (United States Air Force) test target shows vertical and horizontal line triples decreasing in size from 4 line pairs (LP) mm^{-1} down to 228.1 LP mm^{-1}, arranged in seven groups of six different patterns. The lithography shows a checkerboard pattern, which serves as a calibration standard for determination of the image distortion through analysis of contacting corner points of multiple squares along the whole field of view. Studied diameters of the monodisperse standards cover a scope from 9.2 µm to 406 µm. Monodisperse water droplets ejected by the generator vary between 860.7 µm and 68.6 µm in size, while the velocities range between 11 m s^{-1} and 24.5 m s^{-1}. Tab. 1 summarizes the specification of monodisperse droplets, test target and glass microspheres. With respect to the USAF

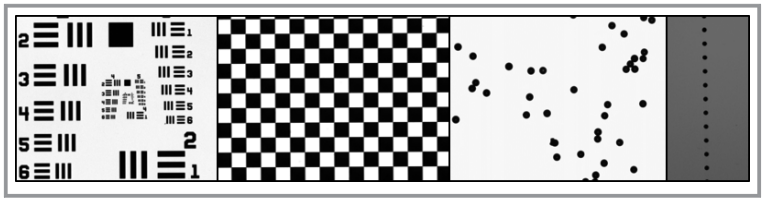

Figure 1. Sample images of USAF test target, lithographic pattern, monodisperse glass particles and liquid monodisperse droplets (left to right).

Table 1. Specification of examined test systems including particle / droplet diameter *d*, droplet velocity *v* and standard deviation *s*.

Monodisperse droplet stream		USAF test target			Monodisperse glass particles	
d [µm]	v [m s^{-1}]	Pattern group	[LP mm^{-1}]	Object size [µm]	d [µm]	s [µm]
68.6	19	2	4	125.0	9.2	0.2
74.5	19	3	8	62.5	25.6	0.7
86.1	24.5	4	16	31.3	40.2	0.5
112.4	21	5	32	15.6	70.9	0.8
120.6	19	6	64	7.8	405.9	8.7
137.1	19	7	128	3.9		
201	11					
352.2	19					
415.3	16.7					
860.7	11					

test target, the table depicts only the largest line triple of each group for reasons of clarity and comprehensibility.

Glass particle diameter d and standard deviation s refer to manufacturer information. Droplet diameter d and velocity v refer to design and operating conditions of the generator provided by the manufacturer. The droplet generator ejects several groups of droplet sizes with different stainless-steel or copper orifices with an opening between 35 µm and 500 µm in diameter. A combination of oscillation frequency and overpressure created by a piezo element and a pressure vessel allows an exact adjustment of the desired droplet size and velocity. The generation of monodisperse droplets is based on the principle of Rayleigh jet breakup. Eq. (1) describes the relation between dimensionless wavelength k, orifice diameter D_o, oscillation frequency f_{os} and velocity v of the droplet [29].

$$k = \frac{\pi D_o f_{os}}{v} \tag{1}$$

The wave generates monodisperse droplets if k equals a value of 0.7. The velocity of the droplet stream depends on the liquid density ρ and the differential pressure Δp [30]. A pressure valve connected to a pressure vessel allows the adjustment of the differential pressure. Eq. (2) describes the relation.

$$v = \sqrt{\frac{2\Delta p}{\rho}} \tag{2}$$

Consequently, the droplet diameter depends on the orifice diameter, the oscillation frequency and the velocity of the droplet stream. Eq. (3) describes the relation [31].

$$d = \left(\frac{3vD_o^2}{2f_{os}}\right)^{1/3} \tag{3}$$

The 1951 USAF test target enables a determination of the optical resolution limit of an image-based measurement system. Images of the test pattern allow an extraction of the grayscale values of the black $GSV^{\min}(f)$ and white lines $GSV^{\max}(f)$ along a line profile for each single line pattern for both probes. The contrast $C(f)$ for each spatial frequency f_{sp}, respectively line triple, can be derived as the quotient of the difference of these grayscale values and their sum by [32]:

$$C(f_{sp}) = \frac{GSV^{\max}(f_{sp}) - GSV^{\min}(f_{sp})}{GSV^{\max}(f_{sp}) + GSV^{\min}(f_{sp})} \tag{4}$$

The modulation transfer function (MTF) is derived by normalizing the local contrast values with the overall image contrast using the brightest and the darkest regions within the acquired image. Eq. (5) provides the definition of the MTF.

$$MTF(f_{sp}) = \frac{C(f_{sp})}{C^{\max}} \tag{5}$$

Fig. 2 illustrates the experimental setup for the examination of monodisperse water droplets ejected by the droplet generator. For lithography, USAF test target and monodisperse glass particle analysis, the same setup (same depth of focus) is used after replacement of the droplet generator.

3.4 Image Acquisition and Analysis

In order to assure constant and comparative test conditions both probes acquire 2500 images at 40 fps and 1 µs exposure time with respect to each measuring point with the droplet generator. The lithographic pattern examination consists of 3498 / 910 chess square detections with respect to the modi-

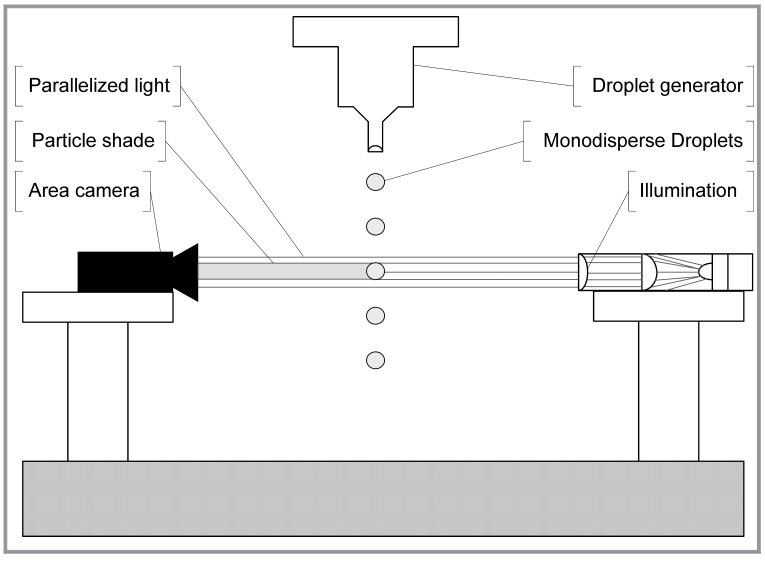

Figure 2. Experimental setup for droplet examination ejected by droplet generator.

fied OMOP / process microscope. The sample of the monodisperse standards contains roughly 500 images leading to a particle number of 100 to 3000 particles per sample depending on particle size and density on each object slide. In case of the modified OMOP, a semiautomatic image analysis with *ImageJ* [33] enables a detailed study of the three test systems. The analysis starts with a threshold operation (Otsu algorithm [34]) and if necessary, with a median filter in order to carefully remove image inequalities caused by dust particles or soiling sticking on the camera sensor. Here, application of a median filter is only useful for particles larger than the respective image inequalities. Consequently, analysis of the smallest particles requires an ideal image quality without any inequalities and with a homogeneous illumination. In scope of this work, the median filter is solely and only if necessary applied during analysis of unmoved test systems as is with glass microspheres, USAF test target and the lithographic pattern. For the fast-moving droplet stream, image inequalities are removed with a background subtraction operation if necessary. The subsequent particle size analysis discards particles, which touch the field of view edges or reach circularities (= $4\pi AP^{-2}$) below 0.5 [33]. The completed analysis specifies each particle in terms of an area equivalent diameter, maximum together with minimum Feret's diameter and circularity. With respect to the Feret's diameter, *ImageJ* selects the maximum or minimum caliper around the particle positioned in any arbitrary angle around the *x*- or *y*-axis [33]. In scope of this work, the maximum Feret's diameter and area equivalent diameter are applied to examine the particles and droplets. Regarding the lithographic pattern, the image distortion is determined with aid of the camera calibration algorithms of *OpenCV*. Due to open source access, fast processing including acceleration of modern hardware and a strong community in research and industry, *OpenCV* is widely used for image processing and computer vision [35]. The algorithm detects the lithographic pattern by finding the chess corners down to the subpixel level. Subsequently, the detected edges are compared with an ideal computer-generated grid of chess squares with 100 µm edge length. The difference between the ideal grid and the acquired image is used to calculate the image distortion. Besides the discrete calculation of this distortion, the software also generates a differential image of the acquired image and the undistorted one. Consequently, a perfect image without any distortion, would lead to a differential image with a background filled completely and solely in black. For visualization purposes, the difference is scaled up by a factor of 20.

4 Experimental Results

4.1 Lithographic Pattern

Figs. 3a and 3b illustrate the search of the image distortion algorithm for the horizontal edges of each chess square and their intersections with respect to the modified OMOP (TUK) and the process microscope (HZDRI). Both images are slightly cropped for equal aspect ratio.

The algorithm is capable of detecting the grid very accurate, which underlines the good acquisition quality of both camera systems. The search for the vertical edges of each chess square and their intersections runs in the same way, shows similar results and is therefore not depicted in this article. Furthermore, a comparison between Fig. 3a and b shows that images acquired by the modified OMOP picture the chess squares smaller than the process microscope. The

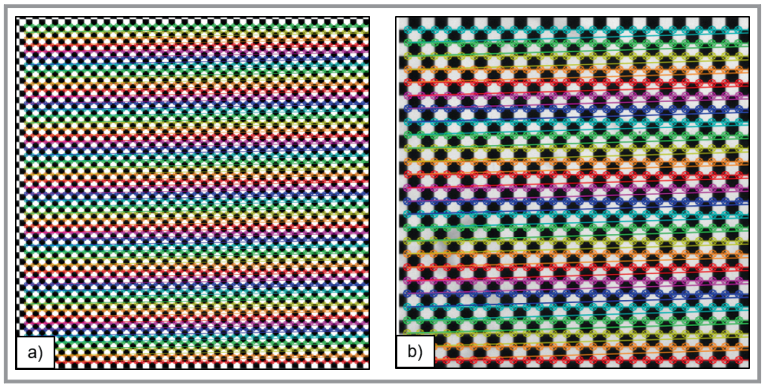

Figure 3. Edge detection of image distortion algorithm in horizontal direction for modified OMOP (a, TUK) and process microscope (b, HZDRI).

reason for that is the larger field of view and smaller pixel size of the modified OMOP. Nevertheless, both probes achieve optimal results with 0.019 % or 0.007 % horizontal and 0.018 % or 0.007 % vertical distortion in case of the modified OMOP or process microscope, respectively. Figs. 4a and 4b demonstrate the distortion in terms of the aforementioned differential image acquired by the captured image and ideal grid with a scale-up factor of 20 for better visualization.

Both differential images show as expected, a low distortion in the image center with increasing distortion values towards the corners. The process microscope shows a large undistorted area slightly off the center and a more pronounced distortion in the lower right corner. The modified OMOP shows an undistorted center with a slightly more equally increasing distortion towards the image corners. In summary, the distortion of the field of view is located in the subpixel range, which underlines the excellent imaging quality of both probes.

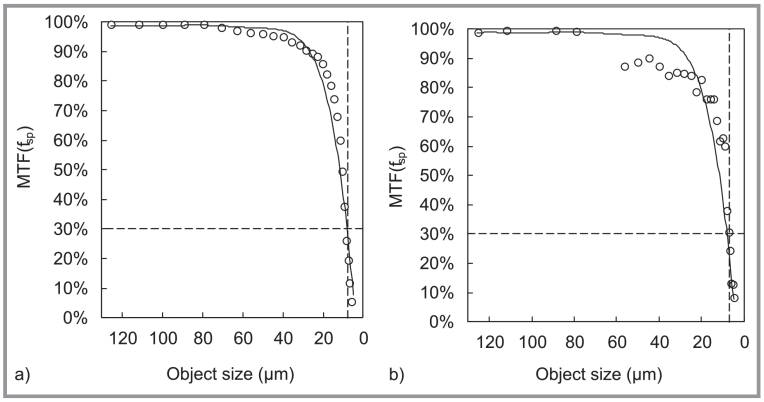

Figure 5. Modulation transfer functions with marking at 30 % contrast ratio for determination of minimum detectable object size derived from 1951 USAF Test Target (a) TUK and b) HZDRI).

4.2 Optical Resolution Limits

Fig. 5 depicts the MTF of both probes. For better recognition of the performance capability, LP mm^{-1} are transferred to minimum detectable object size in µm. The drawn through fitting curve represents an ideal progression of the MTF. A contrast ratio of 30 % between an object with a specific size denoted on the abscissa and the surrounding medium represents the standard minimum MTF for industrial optics.

The results prove that the probes can reliably detect any objects down to 8 µm with respect to the modified OMOP (TUK) and 7 µm in case of the process microscope (HZDRI). In this sense, both systems enable imaging of sprays containing very small droplets, which is of great importance for droplet detection and analysis.

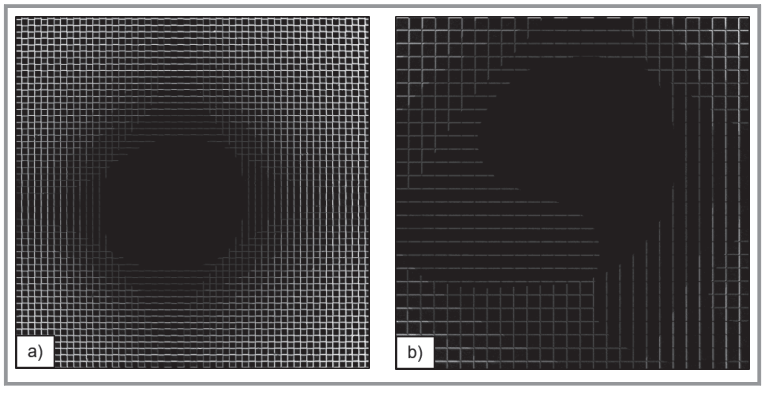

Figure 4. Differential image (20 times amplified) for visualization of the image distortion of the modified OMOP (a, TUK) and process microscope (b, HZDRI).

4.3 Monodisperse Glass Particles

Figs. 6a and 6b delineate the analysis of the monodisperse glass particles in terms of a parity plot detected by the modified OMOP and the process microscope, respectively. The ordinate denotes the experimental particle diameter d_{exp}, while the abscissa refers to the particle diameter provided by the manufacturer d_{man}. Considering statistics, the Feret's diameter and area equivalent diameter refer to arithmetic mean and not to the median value.

The examination of the glass particles shows a good agreement with the provided manufacturer information. The dashed deviation lines visualize a measurement deviation of ± 20 %. Solely the smallest particle size of 9.2 µm exceeds this barrier with respect to the modified OMOP. For example, the smallest particle size of 9.2 µm is detected with a relative measurement deviation ($f_{\bar{x}} = \left|\bar{x}_{exp} - \bar{x}_{man}\right| \bar{x}_{man}^{-1}$) of 30.2 %, while the next larger particle with a diameter of 25.6 µm is detected with a relative measurement deviation of only 3.7 %. Consequently, the deviations steeply fall with increasing particle diameters. The process microscope accurately detects particles down to 25.6 µm ($f_{\bar{x}}$ = 1.5 %) and exceeds a relative measurement deviation of 20 % in case of the smallest particle size of 9.2 µm ($f_{\bar{x}}$ = 27 %). An adjustment of the detection algorithm for the smallest particle size (9.2 µm) represents an opportunity for further improvement of the accuracy. Particles bigger than 16 µm are rejected to isolate single monospheres of the probe and prevent the detection of agglomerated particles, which occur with a higher frequency in the 9.2 µm sample. It is expected that droplets rather form bigger droplets by coalescence than agglomerate as a group of single droplets. This assumption appears reasonable, as the scatter range of the smallest particle is very low according to the manufacturer information (s = 0.2 µm). The constraint of the detec-

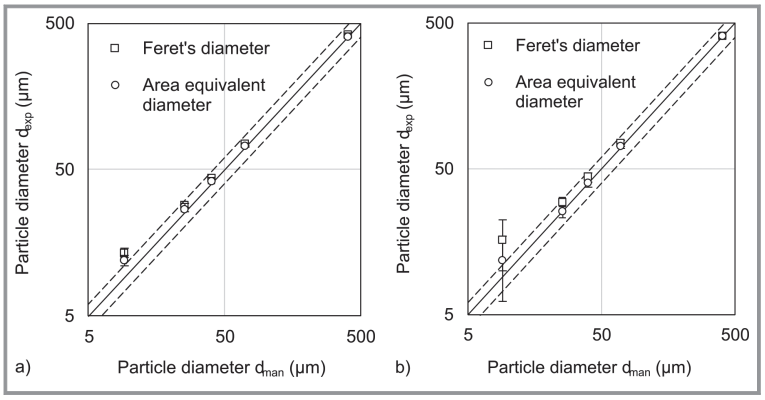

Figure 6. Monodisperse glass particle analysis from 9.2 µm until 406 µm with ±20 % dashed deviation line for modified OMOP (a, TUK) and process microscope (b, HZDRI).

tion range enables an improvement of the accuracy to a relative measurement deviation of 5.1 %. Nevertheless, measurements in industrial practice show mostly higher scatter ranges. Therefore, Fig. 6 depicts the results without algorithm adjustment for an equitable comparison of both systems.

In summary, both probes show an increasing measurement error with decreasing particle size. This imaging limit is reasonable, as the respective sensor pixel size limits the image analysis and the decreasing contrast ratio between particle and surrounding medium impedes a reliable differentiation of particles from the background. Furthermore, the examined test particles reveal higher sizes in case of the Feret's diameter in comparison to the area equivalent diameter. From an image analysis perspective, this behavior is expected and underlines that not all particles of the sample are perfectly round. Nevertheless, the remaining difference may also partly include image distortion, image inequalities and particle agglomeration. Relative measurement deviation of the modified OMOP over all samples amounts to 7.6 % and 14.3 % with respect to the area equivalent diameter and Feret's diameter. Relative measurement deviation of the process microscope over all samples amounts to 5.9 % and 20.8 % in case of the area equivalent diameter and Feret's diameter, respectively.

4.4 Monodisperse Droplet Stream

Figs. 7a and 7b delineate the analysis of the monodisperse droplet stream ejected by the high precision droplet generator in terms of a parity plot with the theoretically calculated droplet diameter d_{th} denoted on the abscissa and the experimentally measured droplet diameter depicted on the ordinate. Again, Feret's diameter and area equivalent diameter refer to the arithmetic mean.

The results show a satisfying agreement between both probes and the theoretical droplet diameter provided by the manufacturer. Even for small droplets below 100 µm, both probes attain high accuracies, although the particle velocities exhibit values up to 24.5 m s^{-1}. Again, droplet sizes determined by Feret's diameter lie slightly above the droplet sizes determined by area equivalent diameter. A natural measurement deviation between probe and droplet generator originates from slight differences in oscillation frequency and overpressure adjustment. Starting from a natural reading error of the overpressure of ± 0.1 bar, the size of the ejected droplets varies in average with + 1.2 % and −1.3 % respectively. The impact of the oscillation frequency is smaller as errors of ± 0.2 Hz result in errors of ± 0.3 %. Hence, not all droplet streams remain completely stable over the whole measurement period, leading to single distorted droplets within a stream, as for instance at the largest droplet size of 860.7 µm. The largest droplet belongs to a group of samples, which are generated with a low overpressure. In this case, 0.6 bar are required for the generation. A low differential pressure reacts more sensitive with respect to the ejected droplet size. For the largest droplet, a natural measurement error of the overpressure of ± 0.1 bar changes the size of the ejected droplets by +2.6 % and −3 % respectively.

In summary, relative measurement deviation of the modified OMOP across all samples amounts to 8.2 % and 5.2 % in case of the area equivalent diameter and Feret's diameter, respectively. Relative measurement deviation of the process microscope across all samples amounts to 6.8 % and 8.1 % in case of the area equivalent diameter and Feret's diameter, respectively. The lower measurement deviation of the droplets compared to the monodisperse glass particles is attributable to the higher droplet sizes. Referring to Tab. 1, the smallest glass particle accounts for a diameter of only 9.2 µm, compared to 68.6 µm with respect to the smallest

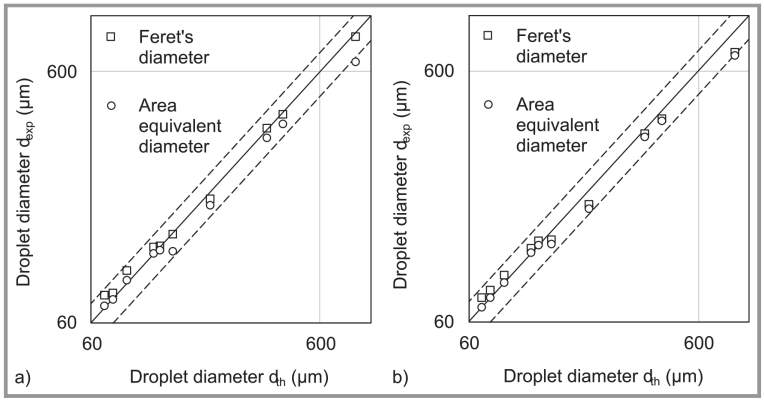

Figure 7. Monodisperse droplet stream analysis from 68.6 µm until 860.7 µm with ±20 % dashed deviation line for modified OMOP (a, TUK) and process microscope (b, HZDRI).

droplet. Nevertheless, the good agreement between both probes and the theoretical diameters provided by the manufacturer remains impressive, most of all due to the aforementioned adjustment differences and the challenge to measure small and by the same time very fast droplets. Furthermore, results show that consideration of several diameter definitions (area equivalent, Feret's or Sauter mean diameter) appears reasonable as the deviations between them allow reasoning on the particle form.

5 Conclusions

Image-based measurement methods for spray detection are scarce but possess a high potential to support and facilitate process analysis and control. The examined test systems underline the capability of modern imaging methods to analyze particle sizes and specifically sprays in a valid and reliable way. Both, the modified OMOP (Technische Universität Kaiserslautern) and the process microscope (HZDR Innovation GmbH) attain satisfying image qualities without relevant distortion. The optical resolution limit of both systems, defined as the minimum object size specified by a MTF of not less than 30 % contrast ratio, amounts to 8 µm for the modified OMOP and 7 µm for the process microscope. Monodisperse glass standards are detected by the modified OMOP and the process microscope with an accuracy of 7.6 % and 5.9 % (area equivalent diameter), respectively. Based on Feret's diameter, the modified OMOP and process microscope reach accuracies of 14.3 % and 20.8 %, respectively. The monodisperse droplets of the droplet generator are detected by the modified OMOP and the process microscope with an accuracy of 8.2 % and 6.8 % (area equivalent diameter), respectively. Based on Feret's diameter the modified OMOP and process microscope reach accuracies of 5.2 % and 8.1 %, respectively. A comparison of Feret's diameter and area equivalent diameter shows as expected higher values in case of the Feret's diameter. For dynamic systems, at laboratory, pilot or industrial scale, a consideration of several diameter definitions appears useful as it reveals more information on the natural lack of roundness of single droplets of the spray. Overall, modern image-based methods are capable of analyzing not even very small but at the same time also fast-moving particles. The ability to even examine sprays by modification of the probe design [4], qualify image-based systems to be a potential contributor to digitalization of modern industrial apparats and plants.

We wish to thank the German Federal Ministry for Economic Affairs and Energy for their financial support and our partners in the joint project TERESA (Tropfenentstehung und Reduzierung in Stoffaustauschapparaten; FKZ 03ET1395H; teresa-projekt.de). Open access funding enabled and organized by Projekt DEAL.

Symbols used

A	[µm^2]	Area
d	[µm]	Particle or droplet diameter
D_c	[mm]	Inner diameter of studied column
D_{pr}	[mm]	Outer diameter of probe
D_o	[µm]	Orifice diameter
f_{os}	[Hz]	Oscillation frequency
f_{sp}	[LP mm^{-1}]	Spatial frequency
$f_{\bar{x}}$	[%]	Deviation from arithmetic means
k	[–]	dimensionless wavelength
Δp	[Pa]	differential pressure
P	[µm]	Perimeter
s	[varies]	Standard deviation
v	[m s^{-1}]	Velocity of droplet
$\bar{x}$	[µm]	Arithmetic mean diameter of particle
ρ	[kg m^{-3}]	liquid density

Abbreviations

EFL	Effective Focal Length
HZDR	Helmholtz Zentrum Dresden-Rossendorf
HZDRI	Helmholtz Zentrum Dresden-Rossendorf Innovation GmbH
LP	Line Pair
MTF	Modulation Transfer Function
OMOP	Optical Multimode Online Probe
TUK	Technische Universität Kaiserslautern
USAF	United States Air Force

Subscripts

exp	Experimental value
man	Manufacturer information
th	Theoretical value

References

[1] A. J. Isaksson, I. Harjunkoski, G. Sand, *Comput. Chem. Eng.* **2018**, *114*, 122–129.
[2] H.-J. Bart, M. W. Hlawitschka, M. Mickler, M. Jaradat, S. Didas, F. Chen, H. Hagen, *Chem. Ing. Tech.* **2011**, *83 (7)*, 965–978. DOI: https://doi.org/10.1002/cite.201100014
[3] S. Maaß, S. Wollny, A. Voigt, M. Kraume, *Exp. Fluids* **2011**, *50 (2)*, 259–269. DOI: https://doi.org/10.1007/s00348-010-0918-9
[4] J. Schulz, H.-J. Bart, *Chem. Eng. Res. Des.* **2019**, *147*, 624–633. DOI: https://doi.org/10.1016/j.cherd.2019.05.041
[5] M. Lichti, J. Schulz, H.-J. Bart, *Chem. Ing. Tech.* **2019**, *91 (4)*, 429–434. DOI: https://doi.org/10.1002/cite.201800045
[6] J. Schulz, K. Schäfer, H.-J. Bart, *Chem. Ing. Tech.* **2019**, *104 (10)*, 202.
[7] M. Lichti, H.-J. Bart, *ChemBioEng Rev.* **2018**, *5 (2)*, 79–89. DOI: https://doi.org/10.1002/cben.201800001
[8] M. Schlüter, *Chem. Ing. Tech.* **2011**, *83 (7)*, 992–1004.

[9] J. Steinhoff, E. Charlafti, L. Reinecke, M. Kraume, H.-J. Bart, *Can. J. Chem. Eng.* **2020**, *98 (1)*, 384–393. DOI: https://doi.org/10.1002/cjce.23603
[10] A. Amokrane, S. Maaß, F. Lamadie, F. Puel, S. Charton, *Chem. Eng. J.* **2016**, *296*, 366–376. DOI: https://doi.org/10.1016/j.cej.2016.03.089
[11] S. Röhl, L. Hohl, M. Kempin, F. Enders, N. Jurtz, M. Kraume, *Chem. Ing. Tech.* **2019**, *91 (11)*, 1640–1655. DOI: https://doi.org/10.1002/cite.201900049
[12] D. Wirz, M. Hofmann, H. Lorenz, H.-J. Bart, A. Seidel-Morgenstern, E. Temmel, *Crystals* **2020**, *10 (9)*, 740. DOI: https://doi.org/10.3390/cryst10090740
[13] G. Lecrivain, G. Petrucci, M. Rudolph, U. Hampel, R. Yamamoto, *Int. J. Multiphase Flow* **2015**, *71*, 83–93. DOI: https://doi.org/10.1016/j.ijmultiphaseflow.2015.01.002
[14] R. Panckow, S. Maaß, J. Emmerich, M. Kraume, *Chem. Ing. Tech.* **2013**, *85 (7)*, 1036–1045. DOI: https://doi.org/10.1002/cite.201200228
[15] M. Lichti, H.-J. Bart, *Flow. Meas. Instrum.* **2018**, *60*, 164–170.
[16] B. Junker, *Bioproc. Biosyst. Eng.* **2006**, *29 (3)*, 185–206. DOI: https://doi.org/10.1007/s00449-006-0070-3
[17] W. V. Pinczewski, C. J. D. Fell, *Trans. Inst. Chem. Eng.* **1977**, *55*, 46–52.
[18] J. Chen, Y. Liu, T. Tan, *Ind. Eng. Chem. Res.* **1999**, *38 (6)*, 2505–2509. DOI: https://doi.org/10.1021/ie980519s
[19] M. Lichti, C. Roth, H.-J. Bart, *Patent EP 3067685B1*, **2016**.
[20] M. Lichti, X. Cheng, H. Stephani, H.-J. Bart, *Chem. Eng. Technol.* **2019**, *42 (2)*, 506–511.
[21] W.-H. Zhang, X. Jiang, Y.-M. Liu, *Pattern Recognit. Lett.* **2012**, *33 (12)*, 1543–1548. DOI: https://doi.org/10.1016/j.patrec.2012.03.027
[22] G. Montante, D. Horn, A. Paglianti, *Chem. Eng. Sci.* **2008**, *63 (8)*, 2107–2118. DOI: https://doi.org/10.1016/j.ces.2008.01.005
[23] S. Maaß, J. Rojahn, R. Hänsch, M. Kraume, *Comput. Chem. Eng.* **2012**, *45*, 27–37. DOI: https://doi.org/10.1016/j.compchemeng.2012.05.014
[24] J. Schäfer, P. Schmitt, M. W. Hlawitschka, H.-J. Bart, *Chem. Ing. Tech.* **2019**, *91 (11)*, 1688–1695. DOI: https://doi.org/10.1002/cite.201900099
[25] ISO 13322-1:2014, *Particle size analysis – Image analysis methods: Part 1: Static image analysis*, International Organization for Standardization, Geneva **2014**.
[26] ISO 13322-2:2006, *Particle size analysis – Image analysis methods: Part 2: Dynamic image analysis methods*, International Organization for Standardization, Geneva **2006**.
[27] M. Mickler, B. Boecker, H.-J. Bart, *Flow. Meas. Instrum.* **2013**, *30*, 81–89. DOI: https://doi.org/10.1016/j.flowmeasinst.2013.01.004
[28] J. Schulz, H.-J. Bart, *Chem. Eng. Trans.* **2018**, *69*, 751–756. DOI: https://doi.org/10.3303/CET1869126
[29] R. S. Donnelly, W. Glaberson, *Proc. R. Soc. London, Ser. A* **1966**, *290 (1423)*, 547–556. DOI: https://doi.org/10.1098/rspa.1966.0069
[30] G. Brenn, *Chem. Eng. Sci.* **2000**, *55 (22)*, 5437–5444. DOI: https://doi.org/10.1016/S0009-2509(00)00167-6
[31] G. Brenn, F. Durst, C. Tropea, *Part. Part. Syst. Charact.* **1996**, *13 (3)*, 179–185. DOI: https://doi.org/10.1002/ppsc.19960130303
[32] DIN IEC 61262-7:1995, *Medical electrical equipment – Characteristics of electro-optical X-ray image intensifiers - Part 7: Determination of the modulation transfer function*, Beuth Verlag, Berlin **2002**.
[33] W. S. Rasband, *ImageJ*, Bethesda, MD **1997**. http://imagej.nih.gov/ij/
[34] N. Otsu, *IEEE T SYST MAN CY-S* **1979**, *9 (1)*, 62–66.
[35] I. Culjak, D. Abram, T. Pribanic, H. Dzapo, H. Cifrek, in *Proc. of the 35th Int. Convention MIPRO*, IEEE, Piscataway, PA **2012**.
[36] M. Lichti, X. Cheng, H. Stephani, H.-J. Bart, Online Detection of Ellipsoidal Bubbles by an Innovative Optical Approach. *Chem. Eng. Technol.* **2019**, *42 (2)*, 506–511. DOI: https://doi.org/10.1002/ceat.201800340

